Synthesis and electrochemical properties of xLiFePO$_4\cdot(1 - x)$LiVPO$_4$F composites prepared by aqueous precipitation and carbothermal reduction

Yi-Chuan Lin [a], George Ting-Kuo Fey [a,*], Pin-Jiun Wu [b], Jeng-Kuei Chang [a], Hsien-Ming Kao [c]

[a] Department of Chemical and Materials Engineering, National Central University, Chung-Li 32054, Taiwan, ROC
[b] National Synchrotron Radiation Research Center, Hsinchu 30075, Taiwan, ROC
[c] Department of Chemistry, National Central University, Chung-Li 32054, Taiwan, ROC

HIGHLIGHTS

- The operating voltage of LFP–LVPF composites for x:$(1 - x)$ = 0.75:0.25, 0.5:0.5 or 0.25:0.75 is higher than that of LFP.
- The mole fraction of LiVPO$_4$F has a dramatic effect on the electrochemical properties.
- Vanadium atoms could be doped into the LiFePO$_4$ structure during the synthesis process.
- The Li$^+$ diffusion coefficient in the LiFePO$_4$ electrode is larger than that in LiVPO$_4$F.

ARTICLE INFO

ABSTRACT

Phosphate-based compounds with the high working voltage, such as Li$_3$V$_2$(PO$_4$)$_3$, LiVPO$_4$F and LiMnPO$_4$, have been proposed as a new class of cathode materials for lithium-ion batteries. To improve the operating voltage of LiFePO$_4$, we introduce LiVPO$_4$F to prepare xLiFePO$_4\cdot(1 - x)$LiVPO$_4$F (LFP–LVPF) composites through an aqueous precipitation and carbothermal reduction method. A series of LFP-LVPF composites have been characterized by X-ray diffraction (XRD), scanning electron microscopy (SEM) and total organic carbon (TOC) analysis. The discharge capacity of LFP–LVPF composites for x:$(1 - x)$ = 1:0, 0.99:0.01, 0.75:0.25, 0.5:0.5, 0.25:0.75 and 0:1 at a 0.2 C-rate is 153, 160, 132, 106, 92 and 78 mAh g^{-1}, respectively. The discharge capacity decreases with increasing mole fraction of LVPF. Moreover, the operating voltage of LFP-LVPF composites for x:$(1 - x)$ = 0.75:0.25, 0.5:0.5 or 0.25:0.75 is higher than that of LFP, and the charge/discharge plateaus around 4.35/4.15 V for LFP-LVPF composites become longer as the value of x decreases.

1. Introduction

Since phospho-olivine polyanionic compound as a potential cathode material were first demonstrated by Goodenough et al., in 1997 [1], LiMPO$_4$ (M = Mn, Fe, Co, Ni) has attracted broad interest as cathode materials for lithium ion batteries. Among all these isostructural compounds, LiFePO$_4$/C composite exhibits good thermal stability, high rate-performance, environmentally friendly properties, and a theoretical capacity of 170 mAh g^{-1} with a flat discharge potential at 3.3 V vs. Li$^+$/Li. However, the operating voltage of LiFePO$_4$ is relatively lower than LiCoO$_2$, LiMn$_2$O$_4$, and LiNi$_{1/3}$Co$_{1/}$

$_3$Mn$_{1/3}$O$_2$ for the practical application. In order to raise the working voltage, many olivine-type cathode materials such as LiMn$_x$Fe$_{1-x}$PO$_4$ and LiCo$_x$Fe$_{1-x}$PO$_4$ have been studied [2–5], due to the redox potentials of Mn^{2+}/Mn^{3+} and Co^{2+}/Co^{3+} which are 4.1 V and 4.9 V, respectively. Recently, phosphate-based compounds with high working voltage, such as Li$_3$V$_2$(PO$_4$)$_3$ [6,7], LiVPO$_4$F [8,9], and LiMnPO$_4$ [10,11], have been proposed as a new class of cathode materials for lithium-ion batteries. Phosphate-based lithium ion batteries may have better performance and safety characteristics than metal oxide batteries because phosphate-based cathode materials possess a structural advantage that limits the likelihood of oxygen liberation and combustion [1,2,9,12].

Lithium manganese phosphate, LiMnPO$_4$, exhibits a high theoretical energy density of 684 Wh kg^{-1} and a high intercalation potential of 4.1 V corresponding to the Mn^{2+}/Mn^{3+} redox couple

[11]. The lithium ion diffusion of olivine-structured $LiMnPO_4$ occurs along a one-dimensional path parallel to the b axis. However, $LiMnPO_4$ has poor electronic conductivity and a low lithium ion diffusion coefficient, which is similar to $LiFePO_4$. Monoclinic lithium vanadium phosphate, $\alpha-Li_3V_2(PO_4)_3$, exhibits a high theoretical capacity of 499.7 Wh kg^{-1} and four redox plateaus around 3.62, 3.68, 4.08, and 4.55 V [13,14]. $Li_3V_2(PO_4)_3$ with three-dimensional (3D) framework consists of a corner shared VO_6 octahedra and PO_4 tetrahedra with three independent lithium sites [6,7], which resulted in higher Li-ion diffusion coefficient and intercalation potentials compared to one-dimensional $LiFePO_4$ [14]. Lithium vanadium fluorophosphate, $LiVPO_4F$, with a potential voltage of 4.2 V versus lithium was proposed by Barker et al. [8], and has attracted specific interest as a highly promising cathode material. The $LiVPO_4F$ compound is isostructural with the naturally occurring mineral tavorite, $LiFePO_4 \cdot OH$, crystallizing with a triclinic structure [8]. The thermal stability of the $LiVPO_4F$ is better than that of oxide-based cathode materials, such as $LiMn_2O_4$, $LiNiO_2$, $LiCoO_2$ [9].

$LiFe_{1-x}Mn_xPO_4$ ($0 \leqq x \leqq 1$) solid solution has recently become one of the promising cathode materials due to its the relative high potential between 3.5 and 4.2 V, which can generate higher energy density especially with greater Mn content [4,15]. Yamada et al. reported that $LiFe_{0.4}Mn_{0.6}PO_4$ exhibited better capacity and good cycling performance [16]. Some research have shown that $LiFe_{1-x}Mn_xPO_4$ prepared by conventional synthesis methods had decreased capacity at higher Mn/Fe ratios ($0.75 \leqq x \leqq 1.0$) [15–17]. On the other hand, Yang et al. [18] also reported that the introduction of large amount of vanadium substitution can form a more electronically conductive phase, $Li_3V_2(PO_4)_3$, in the well-crystallized $LiFePO_4$. Zheng et al. [19] applied an aqueous precipitation of $FeVO_4 \cdot xH_2O$, following chemical reduction and lithiation methods to synthesize a series of $LiFePO_4–Li_3V_2(PO_4)_3$ composites. The two component $LiFePO_4–Li_3V_2(PO_4)_3$ material showed higher operation voltage compared to the redox plateau (3.4 V) of individual $LiFePO_4/C$ composite.

$LiFePO_4$ materials synthesized by using amorphous $FePO_4 \cdot xH_2O$ obtained by spontaneous precipitation have been proposed in other literature [20–23]. Giorgetti et al. applied the XAS technique to study the local structure arrangements of submicrocrystalline $LiFePO_4$ material prepared by a simple sol–gel precipitation during the synthesis steps [23]. In this study, we introduced $LiVPO_4F$ to prepare $xLiFePO_4 \cdot (1 - x)LiVPO_4F$ composites through an aqueous precipitation and carbothermal reduction method, and their material characterization and electrochemical properties were studied.

2. Experimental

2.1. Synthesis of amorphous $FePO_4$

Amorphous iron phosphate ($FePO_4$) was synthesized by spontaneous precipitation from aqueous solutions [20]. Iron (II) sulfate heptahydrate ($FeSO_4 \cdot 7H_2O$) and phosphoric acid (H_3PO_4) were dissolved in de-ionized water to obtain 0.4 mol L^{-1} solution, respectively. An equimolar solution of H_3PO_4 was added to a solution of $FeSO_4 \cdot 7H_2O$ at ambient temperature under stirring. The concentrated hydrogen peroxide (H_2O_2) solution was slowly added to the mixed solution to form a milk-white precipitate, and the molar ratio of H_2O_2 and $FeSO_4$ was 1.2:2. Simultaneously, the concentrated ammonium hydroxide solution (NH_4OH) was dropped into the solution to control the pH at 3.0 ± 0.2. The precipitate was filtered by G4 sand filter funnel and washed several times with distilled water. After dried in an oven at 80 °C for 12 h, yellowish-white amorphous $FePO_4$ was obtained.

2.2. Synthesis of $xLiFePO_4 \cdot yLiVPO_4F$ composites

Stoichiometric amounts of amorphous $FePO_4$, lithium carbonate (Li_2CO_3), Vanadium oxide (V_2O_5), ammonium dihydrogen phosphate ($NH_4H_2PO_4$), Lithium fluoride (LiF) and steric acid (20.0 g $C_{18}H_{36}O_2$/1 mol $FePO_4$) were mixed by ball-milling with a rotation speed of 200 rpm for 0.5 h in alcohol. The resulting mixture was dried at 60 °C to form the dry precursors, and then calcined at 600 °C in a tube furnace for 4.0 h under argon flow. Finally, the $xLiFePO_4 \cdot (1 - x)LiVPO_4F$ composites were obtained. Furthermore, $xLiFePO_4 \cdot (1 - x)LiVPO_4F$ composites for x:$(1 - x)$ = 1:0, 0.99:0.01, 0.75:0.25, 0.5:0.5, 0.25:0.75 and 0:1 are denoted and listed in Table 1. The mole fraction of $LiVPO_4F$ in the $xLiFePO_4 \cdot (1 - x)LiVPO_4F$ composites is equal to $(1 - x)$ divided by 1.0.

2.3. Material characterization

Synchrotron XRD experiments were performed at the BL-01C1 of the National Synchrotron Radiation Research Center (NSRRC), Taiwan. All diffraction patterns in this study were collected using an imaging plate and a wavelength of 0.10332 nm was selected for the measurements. A Rietveld refinement using the General Structure Analysis System (GSAS) software suite was carried out to obtain information about crystal structure. Field-emission scanning electron microscope (FE-SEM, Hitachi S-3500V) was used to observe particle morphology. The resistivity of samples was measured by four-point conductivity measurements with a Keithley Model 2400S source meter. Each sample weighed about 0.2 g, and was pressed into pellets under 10 tons cm^{-2} pressure. According to the Ven der Pauw method: $\sigma = \ln 2 \times \pi^{-1} \times t^{-1} \times R^{-1}$ [24], the resistivity, R, and thickness, t, of samples were used to evaluate the electronic conductivity, σ. The carbon content in LFP–LVPF composites was determined by total organic carbon (TOC) analysis. TOC measurements were conducted using a OIA Model Solids module, which was based on the combustion of organics and detection of CO_2 formed by the infrared gas analysis method. The CO_2 concentration of the sample was measured with a non-dispersive infrared gas analyzer (NDIR), which result was compared to the calibration curve when prepared with standard solutions to determine the

Table 1
Abbreviations and lattice parameters of $xLiFePO_4 \cdot (1 - x)LiVPO_4F$ composites.

Composition[a] $xLiFePO_4 \cdot (1 - x)LiVPO_4F$ x:$(1 - x)$ (mole ratio)	Sample abbreviation	LiFePO$_4$			
		a [Å]	b [Å]	c [Å]	Volume of unit cell [Å^3]
1:0	LFP	10.3324(4)	6.0137(2)	4.7074(2)	292.50(2)
0.99:0.01	LFP-LVPF ($x = 0.99$)	10.3287(3)	6.0117(2)	4.7066(2)	292.25(2)
0.75:0.25	LFP-LVPF ($x = 0.75$)	10.3192(4)	6.0020(2)	4.7004(2)	291.13(2)
0.5:0.5	LFP-LVPF ($x = 0.5$)	10.3179(10)	6.0030(5)	4.6999(4)	291.11(5)
0.25:0.75	LFP-LVPF ($x = 0.25$)	10.3184(10)	6.0029(5)	4.6998(4)	291.11(4)
0:1	LVPF	–	–	–	–

[a] The $xLiFePO_4 \cdot (1 - x)LiVPO_4F$ composites were prepared by aqueous precipitation and carbothermal reduction methods.

carbon content. The tap density of LFP–LVPF composites was determined by a tapping tester (Shin Kwang Machinery Industry Co. Ltd.). After measuring the weight of the powder, the cylinder filled with the powder was fixed on the desk. The vibration desk vibrated vertically at a tapping rate of 85 times per minute with an amplitude of 2 cm, and the cylinder tapped approximately 1000 times. The tap density of samples was calculated using the weight and volume of the powder.

2.4. Electrochemical characterization

The cathodes were prepared by mixing 75 wt% active materials with 20 wt% conductive carbon black and 5 wt% poly(vinylidene fluoride) in a N-methyl-2-pyrrolidone (NMP) solvent, which was then applied onto an etched aluminum foil current collector and dried at 393 K for 12 h in an oven. Lithium metal (Foote Mineral) was used as the anode and 1 M solution of $LiPF_6$ in ethylene carbonate (EC)/diethyl carbonate (DEC) (1:1, v/v) (Tomiyama Chemicals) was used as the electrolyte with a Celgard membrane as the separator. Finally, the CR2032 coin cells were assembled in a glove box filled with argon gas. The cells were galvanostatically cycled at a current of 0.2 C with cut-off voltages of 2.0 and 4.6 V (versus Li/Li^+) at 298 K in a multi-channel battery tester (Maccor 4000).

Cyclic voltammetric measurements were performed on the Li-ion coin cell to identify the characteristics of the redox reactions using a Solartron 1287 Electrochemical Interface with a scan rate of $0.05-1.0$ mV s^{-1} between 2.0 and 4.6 V. The cells were assembled inside a glove box with lithium metal foil as the counter and the reference electrode. The working electrode was the $LiFePO_4$ cathode electrode prepared by the above slurry coating procedure with a dimension of 1.33 cm^2, and the electrolyte was the same as that for the coin cell.

3. Results and discussion

3.1. X-ray diffraction

Fig. 1 shows the XRD patterns of two-component $xLiFePO_4\cdot(1-x)LiVPO_4F$ powders with different mole ratios of $x:(1-x)$. For $x = 1$, the diffraction pattern exhibits a pure phase of $LiFePO_4$, corresponding to an ordered olivine structure indexed in orthorhombic Pnma [1]. For $x:(1-x) = 0.99:0.01$, there are no second phases or impurities found in the diffraction pattern, as shown in
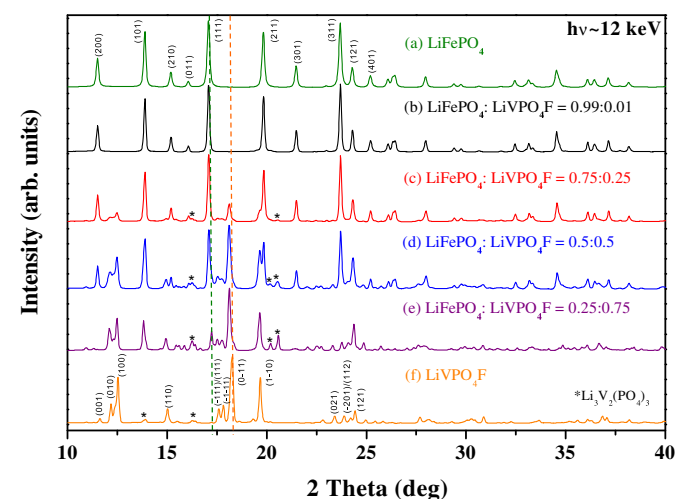
Fig. 1(b). The co-existing phases of $LiFePO_4$ and $LiVPO_4F$ are observed for the LFP–LVPF ($x = 0.75$, 0.5 and 0.25) composites in Fig. 1(c)–(e), respectively, where the $LiVPO_4F$ phase is indexed on the basis of a triclinic structure [8]. As the mole fraction of LVPF is increased, the XRD peaks of LFP phase become weaker and are completely vanished at $x = 0$. On the contrary, the reflection intensity of the LVPF phase gradually increases with an increase in the mole fraction of LVPF. The $Li_3V_2(PO_4)_3$ impurities obviously exist in the LVPF compound, but their diffraction intensities are rather weak. Furthermore, the impurity of $Li_3V_2(PO_4)_3$ is also formed on the LFP–LVPF ($x = 0.75$, 0.5 and 0.25) composites, as shown in Fig. 1(c)–(f), which could be attributed to the monoclinic $Li_3V_2(PO_4)_3$ phase induced by the loss of VF_3 from the sublimation of the reaction mixture [25–27].

Fig. 1. XRD patterns of $xLiFePO_4\cdot(1-x)LiVPO_4F$ composites with different mole ratios of $x:(1-x)$: (a) 1:0; (b) 0.99:0.01; (c) 0.75:0.25; (d) 0.5:0.5; (e) 0.25:0.75 (f) 0:1.
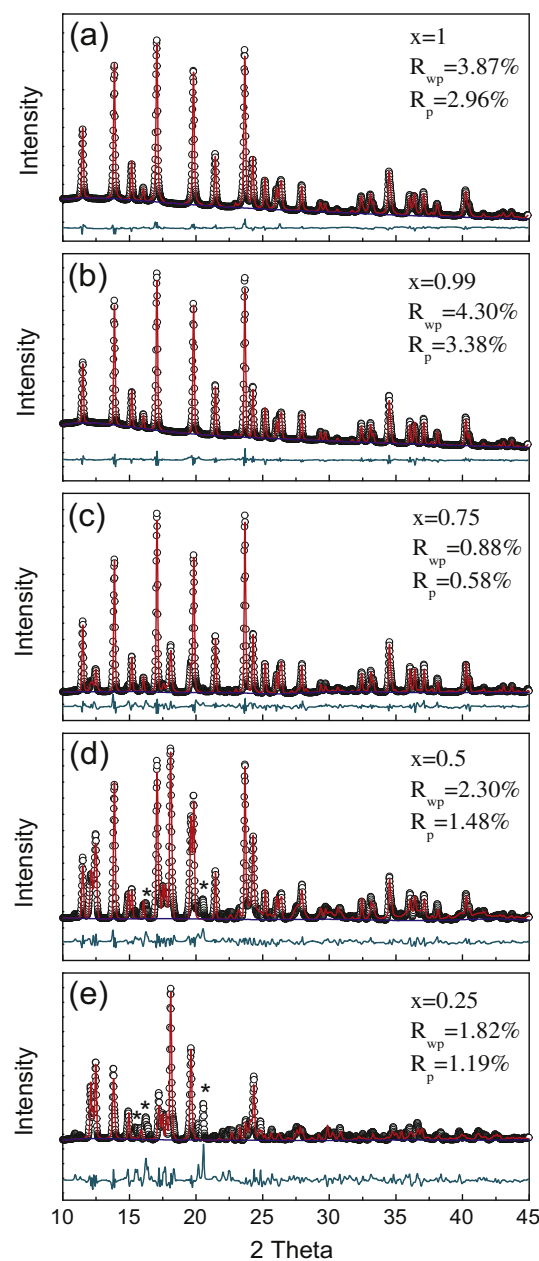

Fig. 2. Rietveld refinements of $xLiFePO_4\cdot(1-x)LiVPO_4F$ composites with different mole ratios of $x:(1-x)$: (a) 1:0; (b) 0.99:0.01; (c) 0.75:0.25; (d) 0.5:0.5; (e) 0.25:0.75. The peaks labeled with an asterisk are due to the $Li_3V_2(PO_4)_3$ impurity.

The observed and calculated XRD patterns of LFP, LVPF, and LFP−LVPF samples are presented in Fig. 2, while the lattice parameters of LFP phase for all samples obtained by the Rietveld refinement method are listed in Table 1. For the LFP−LVPF sample of $x = 0.99$, all three axes of the unit cell of LFP phase shrink compared with pure LFP, indicating a decrease in its cell volume via vanadium modification [28]. The unit cell volume of LFP phase for LFP−LVPF samples of $x = 0.75$, 0.5, and 0.25 is decreased further by increasing doping content and remains almost the same due to doping saturation. The V dopant solubility limit could be obtained somewhat more than 1% in the composition range of $x = 0.99$ to $x = 0.75$. The ionic radii of V^{3+} and V^{5+} are 0.64 and 0.54 Å, respectively, whereas that of Fe^{2+} is 0.78 Å [29]. The reduction of the lattice parameters implies that vanadium atoms were doped into the $LiFePO_4$ matrix structure, which can be attributed to the ionic radius of V^{3+} (0.64 Å) being smaller than that of Fe^{2+} (0.78 Å). In addition, Zheng [13] and Zhang [30] reported that $LiFePO_4$ doped with V^{3+} and $Li_3V_2(PO_4)_3$ doped with Fe^{2+} can both enhance their electronic conductivity and electrochemical performance for the two component $LiFePO_4$−

$Li_3V_2(PO_4)_3$ powders. The incorporation of vanadium can result in a higher electronic conductivity [28,30,31], and consequently the V-doped LFP exhibits a better discharge capacity than pristine LFP, as shown later in the electrochemical properties section.
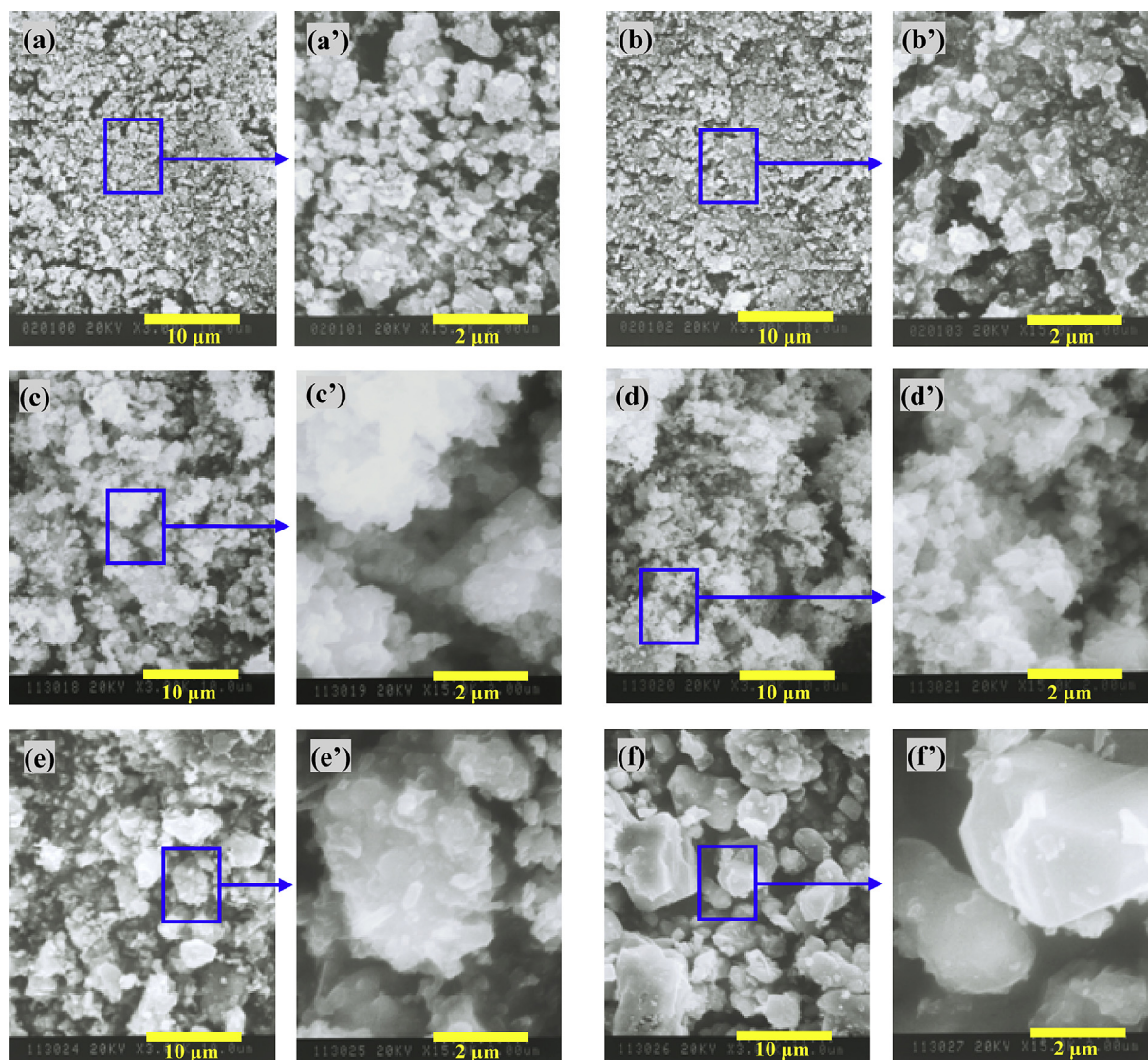
Table 2
A comparison of the tap density, carbon content, particle size, electronic conductivity and specific discharge capacity of $xLiFePO_4 \cdot (1 − x)LiVPO_4F$ composites.

Sample	(A) Electronic conductivity, (S cm^{-1})	(B) Carbon content (wt%)	(C) Tap density (g cm^{-3})	(D) Gravimetric specific discharge capacity^a (mAh g^{-1})
LFP	3.72×10^{-5}	3.21	0.65	156
LFP−LVPF ($x = 0.99$)	5.66×10^{-5}	3.26	0.63	160
LFP−LVPF ($x = 0.75$)	2.95×10^{-6}	2.68	0.70	141
LFP−LVPF ($x = 0.5$)	8.32×10^{-7}	2.06	0.74	108
LFP−LVPF ($x = 0.25$)	7.08×10^{-8}	1.63	0.85	93
LVPF	2.19×10^{-8}	1.35	0.92	78

^{a} The initial discharge capacity was performed at 0.2 C-rate with cut-off voltages of 2.0 and 4.6 V.

Fig. 3. SEM images of $xLiFePO_4 \cdot (1 − x)LiVPO_4F$ composites with different mole ratios of $x:(1 − x)$: (a) 1:0, (b) 0.99:0.01; (c) 0.75:0.25; (d) 0.5:0.5; (e) 0.25:0.75 (f) 0:1; Fig. 3(a′), (b′), (c′), (d′) (e′) and (f′) are partial enlargements of Fig. 3(a), (b), (c), (d), (e) and (f), respectively.

3.2. Morphology

Fig. 3(a)−(f) shows the morphology of xLiFePO$_4$·$(1 − x)$ LiVPO$_4$F composites prepared by an aqueous precipitation and carbothermal reduction method at 873 K for 4.0 h. Fig. 3(a′), (b′), (c′), (d′), (e′) and (f′) are the corresponding partial enlargements of Fig. 3(a), (b), (c), (d), (e) and (f), respectively. For the most part, the formation of nano or submicron sized LiFePO$_4$ particles is much easier when prepared using an aqueous precipitation method

compared with the other solid−state reaction methods [20−23]. From Fig. 3(a) and (b), the pristine LFP and LFP-LVPF ($x = 0.99$) composites have a small particle-size distribution between 200 nm and 1.0 μm, and their surfaces are rough and irregular. However, an LVPF sample synthesized by a carbothermal reduction method exhibits a smooth surface with relatively large particles in the size range between 2.0 and 10 μm, as shown in Fig. 3(f). In particular, the particle size of LFP-LVPF composites increases with increasing mole fraction of LVPF.

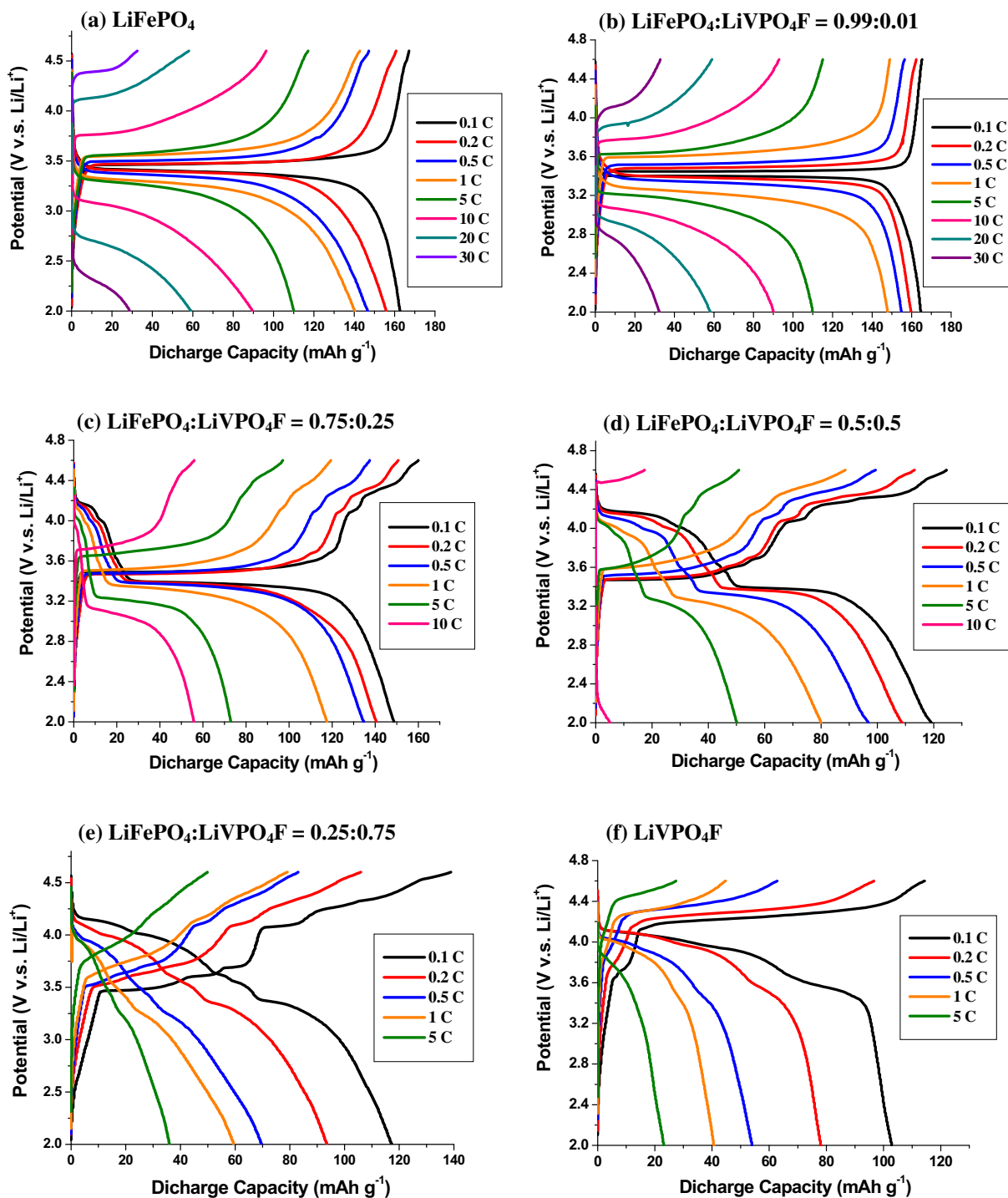**Fig. 4.** The charge/discharge characteristics of xLiFePO$_4$·$(1 − x)$LiVPO$_4$F composites with different mole ratios of x:$(1 − x)$ at different C-rates: (a) 1:0, (b) 0.99:0.01; (c) 0.75:0.25; (d) 0.5:0.5; (e) 0.25:0.75 (f) 0:1.

3.3. Tap density, electronic conductivity and residual carbon content

The electronic conductivity measured by a four-point conductivity method, tap density determined by a tapping tester, and residual carbon content analyzed by TOC measurements for the as-prepared samples are summarized in Table 2. The electronic conductivity and residual carbon content of xLiFePO$_4$·$(1 - x)$LiVPO$_4$F composites decrease with an increase of the mole fraction of LVPF, which indicates that pristine LVPF composite has the intrinsic disadvantage of low electronic conductivity. The residual carbon content of LVPF composite prepared by a carbothermal reduction method using the previously mentioned synthesis conditions was only 1.35 wt%, leading to a reduction in the electronic conductivity. The tap density of LVPF sample is obviously higher than that of the LFP sample, because the LVPF sample exhibits a relatively larger particle size, as shown in Fig. 3(a) and (f). As the mole fraction of LVPF increased from 0 to 1.0, both tap density and particle size increased significantly. In contrast, the initial discharge capacity of the LFP-LVPF composites decreased when the number of moles of LVPF increased, probably due to the lower electronic conductivity of LVPF and residual carbon content.

3.4. Electrochemical properties

The specific capacities of samples were measured by a constant current charge/discharge test between 2.0 and 4.6 V (vs Li$^+$/Li). The charge/discharge characteristics of xLiFePO$_4$·$(1 - x)$LiVPO$_4$F composites at different C-rates are shown in Fig. 4. A couple of charge/discharge plateaus were around 3.50/3.39 V in Fig. 4(a) for intercalation/deintercalation of Li$^+$ into/from LiFePO$_4$, while the other typical charge/discharge plateaus were around 4.35/4.15 V in Fig. 4(f) for intercalation/deintercalation of Li$^+$ reversibly into/from LiVPO$_4$F based on the V^{3+}/V^{4+} redox couple. Among LFP–LVPF composites, the LFP–LVPF ($x = 0.99$) composite demonstrated the best discharge capacity with a flat discharge plateau at about 3.4 V vs. Li/Li$^+$ and a slight voltage polarization of about 0.06 V between two plateaus at a 0.1 C-rate, as shown in Fig. 4(b). The LFP–LVPF ($x = 0.99$) composite achieved a reversible capacity of 160 mAh g^{-1} at a 0.2 C-rate, which is similar to the capacity reported in other studies [32–34].

From Fig. 4(f), the discharge profile of the LVPF sample shows a voltage plateau at around 4.15 V with a minor step in the relatively low voltage of about 3.6 V, and the total discharge capacity is 103 mAh g^{-1} at a 0.1 C-rate. The main plateau at 4.15 V is due to the LVPF compound, while the minor step at 3.6 V is attributed to the small amount of Li$_3$V$_2$(PO$_4$)$_3$ impurity [25–27]. However, the LVPF sample can only sustain a 5 C charge and discharge rate.

The charge/discharge behavior of LFP-LVPF composites in Fig. 4(c)–(e) shows more complicated profiles, which contain the main plateau near 3.40 V due to LFP and a plausible plateau at around 4.15 V with many minor steps in the relatively low voltage around 3.56 V, 3.64 and 4.03 V due to LVPF. In addition, these minor steps contain few barely visible plateaus due to Li$_3$V$_2$(PO$_4$)$_3$ impurity, as shown in Fig. 4(c)–(e).

According to previous studies [13,14], Li$_3$V$_2$(PO$_4$)$_3$ exhibits three discharge plateaus at around 3.55, 3.65 and 4.05 V at a 0.1 C-rate. As seen in the charge/discharge profiles of the LFP-LVPF ($x = 0.5$ and 0.25) samples, there are not only two charge/discharge plateaus at 3.50/3.39 V and 4.35/4.18 V, which correspond to the Li$^+$ intercalation/deintercalation process of LiFePO$_4$ and LiVPO$_4$F, respectively, but also three minor charge/discharge plateaus around 3.62/3.56, 3.70/3.64, and 4.10/4.03 V for intercalation/deintercalation of two

Li$^+$ reversibly into/from Li$_3$V$_2$(PO$_4$)$_3$ based on the V^{3+}/V^{4+} redox couple are distinctly observed [13,30]. These three charge/discharge plateaus of Li$_3$V$_2$(PO$_4$)$_3$ become more apparent with increasing mole fraction of LVPF. From Fig. 1(c)–(f), the XRD patterns show that LFP-LVPF ($x = 0.75, 0.5$ and 0.25) and LVPF samples all contain a relatively small amount of Li$_3$V$_2$(PO$_4$)$_3$ phase, which could be attributed to the product induced by the loss of VF$_3$ from the sublimation of the reaction mixture [25–27]. The LiVPO$_4$F content has a dramatic effect on the electrochemical properties of LFP–LVPF composites. The average discharge voltage of LFP–LVPF composites increased with increasing mole fraction of LVPF, but capacities decreased gradually at all C-rates except in the case of pristine LFP sample.

The LFP–LVPF ($x = 0.99$) composite shows better cell performance than the other LFP–LVPF ($x < 0.99$) samples, which display 154 and 110 mAh g^{-1} at 0.5 and 5.0 C-rates for the first cycle, respectively, and 50 cycles with a capacity retention of more than 101.6%, as shown in Fig. 5 and Table 3. However, the rate capability and cycling stability of LFP-LVPF composites are reduced significantly with an increase in LVPF content. The initial discharge capacities of LFP–LVPF composites for x:$(1 - x) = 0.75$:0.25, 0.5:0.5, 0.25:0.75 and 0:1 were 73, 50, 35 and 22 mAh g^{-1} at a 5 C-rate in the potential range of 2.0–4.6 V, respectively. Obviously, the samples with higher LVPF content ($x = 0.25$ and 0) show poor rate performance compared with the other ones, corresponding to capacity retention of 17.8% and 15.1% after 50 cycles.
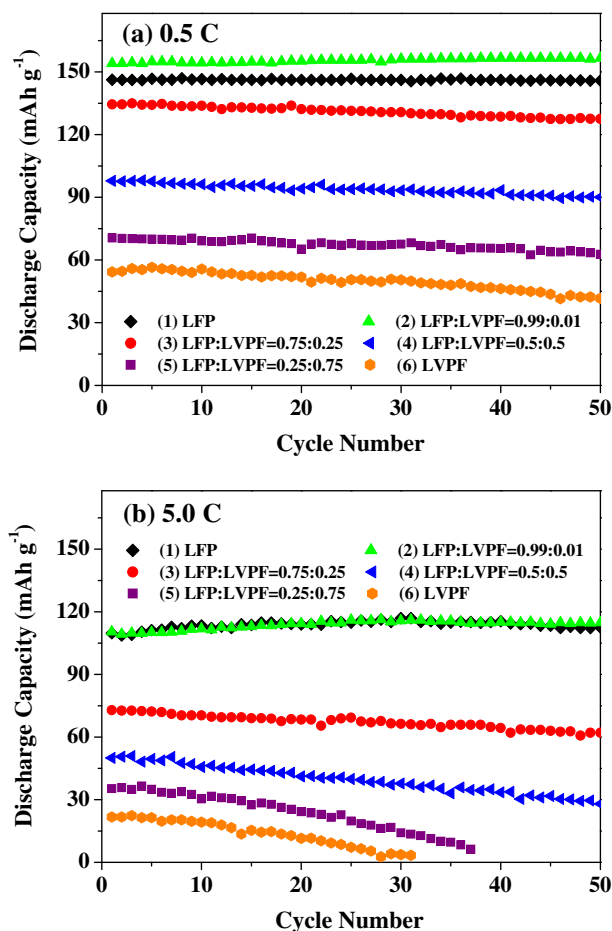

Fig. 5. Cyclic performances of xLiFePO$_4$·$(1 - x)$LiVPO$_4$F composites at the different C rates: (a) 0.5 C, (b) 5.0 C.

Table 3
Discharge capacities of the 1st and the 50th cycles at different C-rates of xLiFePO$_4$·$(1 - x)$LiVPO$_4$F composites.

Sample	0.5 C (mAh g^{-1})			5 C (mAh g^{-1})		
	1st	50th	C.R. (%)[a]	1st	50th	C.R. (%)[a]
LFP	146.3	145.9	99.7	109.7	112.5	102.5
LFP–LVPF ($x = 0.99$)	154.1	156.6	101.6	110.4	114.8	103.9
LFP–LVPF ($x = 0.75$)	134.5	127.5	94.8	72.9	62.1	85.2
LFP–LVPF ($x = 0.5$)	97.9	90.1	92.0	50.0	28.0	56.0
LFP–LVPF ($x = 0.25$)	70.5	62.8	89.1	35.3	6.3	17.8
LVPF	54.3	41.7	76.8	21.8	3.3	15.1

[a] Capacity retention ratios compared to the first cycle.

3.5. Cyclic voltammetry

Cyclic voltammetry (CV) profiles reflect the redox behavior of xLiFePO$_4$·$(1 - x)$LiVPO$_4$F electrodes for x:$(1 - x)$ = 1:0, 0.5:0.5 and 0:1 at different potential scanning rates of 0.05, 0.1, 0.2, 0.5, and 1 mV s^{-1}, as shown in Fig. 6. The presence of only one oxidation/reduction peak at around 3.62/3.25 V indicates that strong lithium intercalation/de-intercalation reaction occurs in the LFP and LFP-LVPF ($x = 0.99$) electrodes. The ΔV values between the anodic and cathodic peaks are 0.33, 0.40, 0.54, 0.69 and 0.77 V, corresponding to scanning rates of 0.05, 0.1, 0.25, 0.5 and 1.0 mV s^{-1}, respectively, indicating that the polarization of the LFP electrode increased with increasing scan rate. Similarly, the ΔV values of LFP-LVPF ($x = 0.99$) electrode also increased as the sweeping rate was raised.

From Fig. 6(d), the main redox potential pairs of the LVPF electrode occur at around 4.38/4.13 V. Two very low-intensity anodic

peaks are observed at 3.62 and 4.09 V, corresponding to a cathodic peak at 3.59 V, which is consistent with the results previously reported for CV measurements of LiVPO$_4$F as a cathode [35,36]. Furthermore, the low-intensity minor anodic/cathodic peaks are similar to the peaks observed in the differential capacity plot of a Li/Li$_3$V$_2$(PO$_4$)$_3$ cell [27]. This indicates that the impurity phase in the XRD patterns is indeed Li$_3$V$_2$(PO$_4$)$_3$, as shown in Fig. 1(f).

From Fig. 6(c), the redox potential peaks of LiFePO$_4$ and LiVPO$_4$F are both observed, which indicates that they coexist in LFP-LVPF ($x = 0.5$) composite. The main anodic/cathodic peaks of LFP and LVPF compounds occurred at around 3.74/3.24 V and 4.36/4.13 V, respectively. In addition, the ΔV values and the current density also increased with increasing the scanning rate. According to the Randles Sevcik equation [37], the redox behavior of electrodes was related to the Li$^+$ diffusion within the active material. The peak current, I_p, during anodic scans at different sweep rates were used to extract the Li$^+$ diffusion coefficient, D_{Li}, of the cathode material using the following equation [37]:

$$I_p = 2.69 \times 105 \times C_{Li} \times A \times n^{3/2} \times D_{Li}^{1/2} \times v^{1/2} \qquad (1)$$

where C_{Li} is the Li$^+$ concentration (mol cm^{-3}), A is the electrode area (cm^2), n is the number of electrons involved in the redox process, v is the potential scan rate (V s^{-1}), I_p is the peak current in amperes, and D_{Li} is the Li$^+$ diffusion coefficient in cm^2 s^{-1}. From Fig. 7, the peak current (I_p) exhibits a linear relationship with the square root of the scanning rate ($v^{1/2}$). Applying the slope values in Fig. 7 to the Eq. (1), the Li$^+$ diffusion coefficients at different voltage stages were calculated, as shown in Table 4. The LFP-LVPF ($x = 0.99$)
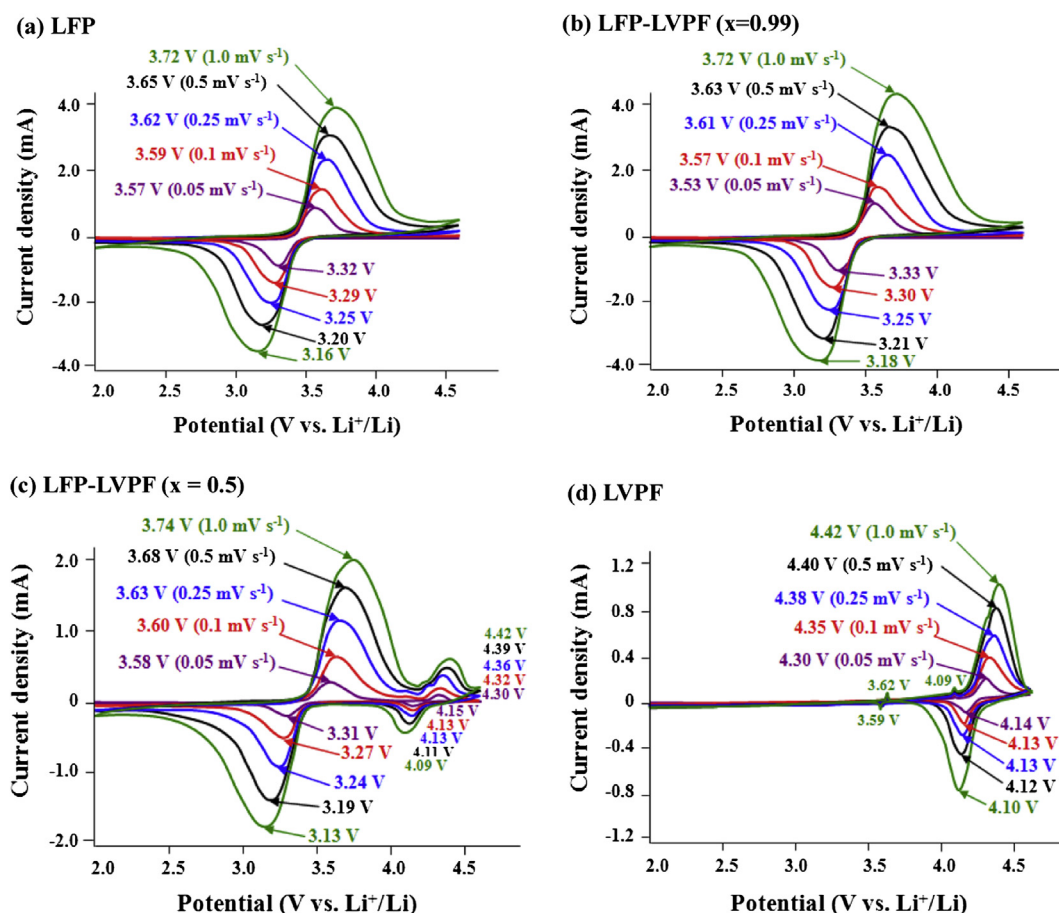
Fig. 6. Cyclic voltammograms of xLiFePO$_4$·$(1 - x)$LiVPO$_4$F electrodes between 2.0 and 4.6 V at different scanning rates: (a) LFP; (b) LFP-LVPF ($x = 0.99$); (c) LFP-LVPF ($x = 0.5$); (d) LVPF.
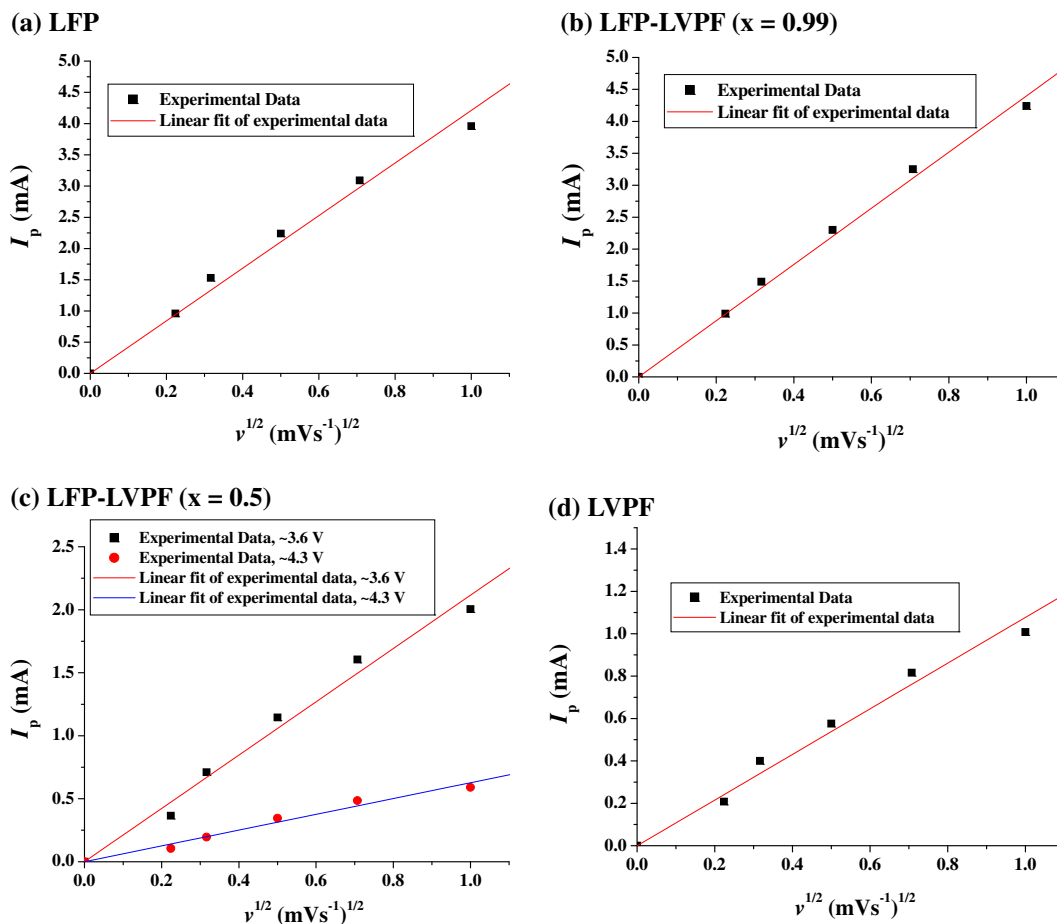
Fig. 7. The plot of the peak current versus square root of scanning rate for xLiFePO$_4$·$(1 - x)$LiVPO$_4$F electrodes: (a) LFP; (b) LFP-LVPF ($x = 0.99$); (c) LFP-LVPF ($x = 0.5$); (d) LVPF.

Table 4
The lithium ion diffusion coefficients of xLiFePO$_4$·yLiVPO$_4$F electrodes for x:$(1 - x)$ = 1:0, 0.99:0.01, 0.5:0.5 and 0:1.

Sample	Lithium ion diffusion coefficient D$_{Li}$ (cm^2 s^{-1})	
	~3.6 V	~4.3 V
LFP	1.44×10^{-11}	–
LFP–LVPF ($x = 0.99$)	1.52×10^{-11}	–
LFP–LVPF ($x = 0.5$)	3.64×10^{-12}	3.19×10^{-13}
LVPF	–	9.43×10^{-13}

electrode has a slightly higher D_{Li} value than that of the LFP electrode. The Li$^+$ diffusion coefficients of the LFP and LFP-LVPF ($x = 0.99$) electrodes are obviously larger than that in the LVPF and LFP-LVPF ($x = 0.5$) electrodes, leading to the better electrochemical performance including the high rate capacity and cycling stability. Due to the low electronic conductivity and Li$^+$ diffusion coefficient of LVPF sample, the electrochemical performance of LFP-LVPF composites is reduced significantly with an increase in the mole fraction of LVPF.

4. Conclusion

xLiFePO$_4$·$(1 - x)$LiVPO$_4$F composites were successfully synthesized by a combination of aqueous precipitation and carbothermal reduction methods. Based on the XRD refinement results, the contraction of the unit cell for the LFP-LVPF ($x = 0.99$)

composite shows that vanadium can be doped into the LiFePO$_4$ matrix structure. The unit cell volume of the LFP phase in the LFP-LVPF ($x = 0.75$, 0.5 and 0.25) composites is significantly smaller than that of the pristine LFP, which may be attributed to the ionic radius of V^{3+} dopant being smaller than that of Fe^{2+} in LiFePO$_4$ crystal. From CV tests and electronic conductivity measurements, it is worth notice that the LVPF compound has relatively low Li$^+$ diffusion coefficient and electronic conductivity compared to the pristine LFP composite, which results in a lower rate capability and poor cycling stability for LFP-LVPF composites with an increase in the mole fraction of LVPF. The LFP-LVPF ($x = 0.99$) composite exhibits outstanding discharge capacity of 160 mAh g^{-1} at a 0.2 C-rate in this study and good cycling stability of 101.6% capacity retention over 50 cycles at a 5.0 C-rate. Furthermore, the operating voltage of LFP-LVPF composites for x:$(1 - x)$ = 0.75:0.25, 0.5:0.5 or 0.25:0.75 is higher than that of LFP, and the charge/discharge plateaus around 4.35/4.15 V for LFP-LVPF composites become longer with increasing mole fraction of LVPF.

References

[1] A.K. Padhi, K.S. Nanjundaswamy, J.B. Goodenough, J. Electrochem. Soc. 144 (1997) 1188–1194.
[2] A. Yamada, M. Hosoya, S.C. Chung, Y. Kudo, K. Hinokuma, K.Y. Liu, Y. Nishi, J. Power Sources 119–121 (2003) 232–238.
[3] C.M. Burba, R. Frech, J. Power Sources 172 (2007) 870–876.
[4] J. Hong, F. Wang, X. Wang, J. Graetz, J. Power Sources 196 (2011) 3659–3663.
[5] D. Wang, Z. Wang, X. Huang, L. Chen, J. Power Sources 146 (2005) 580–583.

[6] S.C. Yin, P.S. Strobel, H. Grondey, L.F. Nazar, Chem. Mater. 16 (2004) 1456–1465.
[7] M. Sato, H. Ohkawa, K. Yoshida, M. Saito, K. Uematsu, K. Toda, Solid State Ionics 135 (2000) 137–142.
[8] J. Barker, R.K.B. Gover, P. Burns, A. Bryan, M.Y. Saidi, J.L. Swoyer, J. Power Sources 146 (2005) 516–520.
[9] R.K.B. Gover, P. Burns, A. Bryan, M.Y. Saidi, J.L. Swoyer, J. Barker, Solid State Ionics 177 (2006) 2635–2638.
[10] T. Drezen, N.H. Kwon, P. Bowen, I. Teerlinck, M. Isono, I. Exnar, J. Power Sources 174 (2007) 949–953.
[11] T. Shiratsuchi, S. Okada, T. Doi, J.I. Yamaki, Electrochim. Acta 54 (2009) 3145–3151.
[12] H.F. Xiang, H. Wang, C.H. Chen, X.W. Ge, S. Guo, J.H. Sun, W.Q. Hu, J. Power Sources 191 (2009) 575–581.
[13] J.C. Zheng, X.H. Li, Z.X. Wang, J.H. Li, L.J. Li, L. Wu, H.J. Guo, Ionics 15 (2009) 753–759.
[14] A. Pan, D. Choi, J.G. Zhang, S. Liang, G. Cao, Z. Nie, B.W. Arey, J. Liu, J. Power Sources 196 (2011) 3646–3649.
[15] S.M. Oh, H.G. Jung, C.S. Yoon, S.T. Myung, Z. Chen, K. Amine, Y.K. Sun, J. Power Sources 196 (2011) 6924–6928.
[16] A. Yamada, S.C. Chung, J. Electrochem. Soc. 148 (2001) A960–A967.
[17] G.H. Li, H. Azuma, M. Tohda, J. Electrochem. Soc. 149 (2002) A743–A747.
[18] M.R. Yang, W.H. Ke, S.H. Wu, J. Power Sources 165 (2007) 646–671.
[19] J.C. Zheng, X.H. Li, Z.X. Wang, S.S. Niu, D.R. Liu, L. Wu, L.J. Li, J.H. Li, H.J. Guo, J. Power Sources 195 (2010) 2935–2938.
[20] Y. Huang, H. Ren, Z. Peng, Y. Zhou, Electrochim. Acta 55 (2009) 311–315.
[21] P.P. Prosini, M. Carewska, S. Scaccia, P. Wisniewski, S. Passerini, M. Pasquali, J. Electrochem. Soc. 149 (2002) A886–A890.
[22] Y. Huang, H. Ren, S. Yin, Y. Wang, Z. Peng, Y. Zhou, J. Power Sources 195 (2010) 610–613.
[23] M. Giorgetti, M. Berrettoni, S. Scaccia, S. Passerini, Inorg. Chem. 45 (2006) 2750–2757.
[24] L.J. Van der Pauw, Philips Res. Rep. 13 (1958) 1.
[25] J. Barker, R.K.B. Gover, P. Burns, A. Bryan, M.Y. Saidi, J.L. Swoyer, J. Electrochem. Soc. 152 (2005) A1776–A1779.
[26] F. Zhou, X. Zhao, J.R. Dahn, Electrochem. Commun. 11 (2009) 589–591.
[27] M.Y. Saidi, J. Barker, H. Huang, J.L. Swoyer, G. Adamson, Electrochem. Solid State Lett. 5 (2002) A149–A151.
[28] J. Hong, X.L. Wang, Q. Wang, F. Omenya, N.A. Chernova, M.S. Whittingham, J. Graetz, J. Phys. Chem. C 116 (2012) 20787–20793.
[29] A. Kelly, K.M. Knowles, Crystallography and Crystal Defects, second ed., John Wiley & Sons, Ltd., New York, 2012. Appendix 7.
[30] L.L. Zhang, G. Liang, A. Ignatov, M.C. Croft, X.Q. Xiong, I.M. Hung, Y.H. Huang, X.L. Hu, W.X. Zhang, Y.L. Peng, J. Phys. Chem. C 115 (2011) 13520–13527.
[31] N. Hua, C. Wang, X. Kang, T. Wumair, Y. Han, J. Alloys Compd 503 (2010) 204–208.
[32] J. Wang, X. Sun, Energy Environ. Sci. 5 (2012) 5163–5185.
[33] W.J. Zhang, J. Power Sources 196 (2011) 2962–2970.
[34] Y. Zhang, Q.Y. Huo, P.P. Du, L.Z. Wang, A.Q. Zhang, Y.H. Song, Y. Lv, G.Y. Li, Synth. Met. 162 (2012) 1315–1326.
[35] M.V. Reddy, G.V. Subba Rao, B.V.R. Chowdari, J. Power Sources 195 (2010) 5768–5774.
[36] Q. Zhang, S. Zhong, L. Liu, J. Liu, J. Jiang, J. Wang, Y. Li, J. Phys. Chem. Solids 70 (2009) 1080–1085.
[37] J.R. Dahn, J.W. Jiang, L.M. Moshurchak, J. Electrochem. Soc. 152 (2005) A1283–A1289.